Structures 79 (2025) 109515

Contents lists available at ScienceDirect

Structures

journal homepage: www.elsevier.com/locate/structures

Effect of high-volume recycled concrete powder on microstructure and mechanical performance of alkali-activated slag mortar using response surface approach

Zhen Zou [a,b], Jingyun Li [b], Jiehong Li [c], Han Gao [c], Yingda Zhang [d], Yang Yu [b,c,*], Chunwei Zhang [b,**]

[a] School of Materials Science and Engineering, Shenyang University of Technology, Shenyang, Liaoning 110870, China
[b] Multidisciplinary Center for Infrastructure Engineering, School of Architecture and Civil Engineering, Shenyang University of Technology, Shenyang, Liaoning 110870, China
[c] Centre for Infrastructure Engineering and Safety, UNSW Sydney, NSW 2052, Australia
[d] School of Architecture and Civil Engineering, Xihua University, Chengdu 610039, China

ARTICLE INFO

Keywords:
Alkali-activated slag mortar
Recycled concrete powders
Response surface method
Microstructure
Mechanical performance

ABSTRACT

To optimize the mix design of high-volume recycled concrete powder (RCP) alkali-activated slag mortar (HRAASM) and improve its mechanical performance, this study utilizes Box-Behnken design-based response surface method (RSM) to evaluate the effects of RCP particle size, activator modulus (Ms), activator content (C), and water to solid ratio (W/S) on mechanical properties of HRAASM. XRD, FTIR, TG-DSC, and SEM are employed to investigate the relationship between compressive strength, reaction products, reaction processes, and microstructure under different mix design parameters. The results reveal that under optimal parameters (RCP size: 15.2 μm, Ms: 1.59, C: 7.42 %, W/S: 0.47), the compressive strength reaches a maximum of 57.5 MPa at 28 days. RCP particles of 15.2 μm promote the formation of amorphous phases (C-S-H/C-A-S-H), while larger RCP particles mainly act as inert fillers. When the Ms is 1.6 and the W/S is 0.46, the interaction reduces matrix porosity and crack formation, thus synergistically enhancing the matrix densification. However, a W/S of 0.5 reduces strength, especially when using 33.6 μm RCP particles. This research provides valuable insights into the high-value recycling of recycled concrete powder and presents a feasible approach for developing alkali-activated slag mortar with enhanced mechanical performance.

1. Introduction

Construction waste is a main part of global waste, with its generation increasing due to urbanization and infrastructure expansion [1]. The United Nations Environment Program reported global waste generation of 2 billion tons in 2016, expected to rise to 2.2 billion tons by 2025 and 2.7 billion tons by 2050. Construction waste accounts for 30–44 % of total global waste [2]. However, the concrete waste recycling rate is under 30 %, resulting in large amounts being landfilled, causing environmental issues such as land degradation [3], greenhouse gas emissions [4], and soil and water contamination [5]. Landfilling exacerbates pollution and strains natural resources, highlighting the need for innovative concrete waste management and recycling solutions in the construction industry.

The construction industry primarily manages waste concrete through resource utilization, focusing on reuse and remanufacturing. Demolished concrete blocks are reused as base materials or fillers for construction projects [6,7]. Waste concrete is also processed into recycled concrete powder (RCP) and recycled concrete aggregate (RCA) through crushing and screening, and used in new concrete, foundations, pavements, and other applications [8,9]. Utilzing recycled aggregate in new concrete is well-established. For example, Zhang et al. [10] used post-fire waste concrete as a coarse aggregate substitute for producing RAC, achieving a compressive strength of 26.31 MPa even with a 100 %

* Corresponding author at: Multidisciplinary Center for Infrastructure Engineering, School of Architecture and Civil Engineering, Shenyang University of Technology, Shenyang, Liaoning 110870, China.
** Corresponding author.
E-mail addresses: yang.yu12@unsw.edu.au (Y. Yu), zhangchunwei@sut.edu.cn (C. Zhang).

https://doi.org/10.1016/j.istruc.2025.109515
Received 3 April 2025; Received in revised form 2 June 2025; Accepted 19 June 2025
Available online 23 June 2025

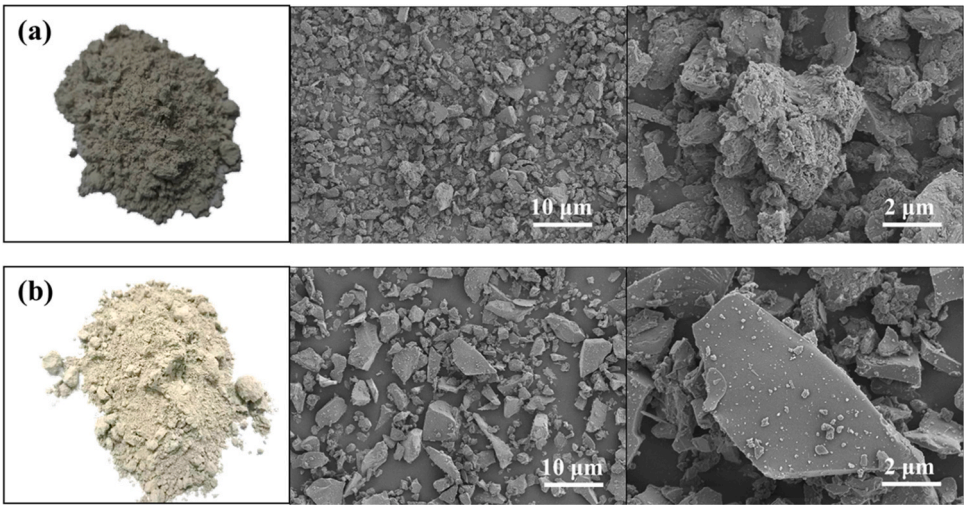

Fig. 1. Appearance and microstructure of raw materials: (a) RCP, (b) GGBFS.

Table 1
Chemical composition and content of materials (mass fraction %).

	SiO_2	Al_2O_3	CaO	Fe_2O_3	SO_3	MgO	K_2O	Na_2O	TiO_2	MnO	LOI*
RCP	39.42	7.82	39.73	4.74	1.46	1.54	1.82	1.37	0.44	0.07	1.24
GGBFS	30.73	15.96	42.26	0.29	0.26	6.66	0.34	0.04	1.34	0.41	1.11

* Loss on ignition

RCA replacement at 800°C. Zhu et al. [11] found that RAC from RCA with a 50 % replacement after two freeze-thaw cycles had a compressive strength of 48.3 MPa, with improved freeze-thaw resistance. Al-Waked et al. [12] enhanced recycled aggregate using methods like sand envelope mixing (SE), soaking in a cement-fly ash-silica fume solution (SCF), and their combination (SCF+SE). The enhanced RAC showed a 46 MPa increase of 28-day compressive strength, with improvements of flexural strength, splitting tensile strength, and elastic modulus by 16 %, 10 %, and 6 %, respectively. RCP, as a secondary product of the resource utilization of construction waste, lags significantly behind RCA in terms of high-value applications. During concrete demolition, RCP can account for up to 25 % of the total mass. However, around 90 % of RCP is still disposed of by landfilling, which not only occupies considerable land area but also poses risks of soil and groundwater contamination through the leaching of heavy metals and alkaline substances [3], posing a potential pollution risk to soil and groundwater ecosystems [5]. While RCP exhibits some pozzolanic activity, its low activity index (typically <70 %) and high compositional variability have limited its use to less than 10 % in most cement-based systems. For example, Mohammad et al. [13] revealed that replacing up to 15 % of cement with RCP did not affect the strength, but higher replacements reduced mechanical properties. Ruth Bola et al. [14] showed that 15 %-25 % RCP in cement met Brazilian standards for C40 and C32 grades, reducing CO_2 emissions by up to 25 %. Wu et al. [15] found that replacing 30 % of cement with recycled fine powder (RFP) reduced hydration products and affected strength and impermeability. RCP replacement is typically limited to 10 %-30 %; beyond that, the concrete performance declines. Ma et al. [16] revealed that using hydrated cement powder (HCP) reduced workability and mechanical strength, with 50 % HCP lowering compressive strength by 50 %. Liu et al. [17] showed that 25 % RCP improved the ductility of UHP-ECC, but 75 % replacement reduced its strength. Wu et al. [18] found that less than 30 % CP in concrete had similar or better strength than ordinary paste, but 70 % CP decreased strength. The low reactivity of RCP limits its high-volume use. RCP, rich in SiO_2, CaO, and Al_2O_3, is less reactive compared to alkali-activated slag (AAS), which uses an alkaline solution to activate slag. Ren et al. [19] demonstrated that substituting 20 % of slag with RCP increased AAS concrete strength by 13 %. Liang et al. [20] found that adding 6 % ultrafine waste concrete powder (UWCP) to AAS improved compressive strength, reaching 86.3 MPa at 56 days. Wang et al. [21] showed that adding 10 %-30 % RCP to GGBFS improved early mortar strength, especially with finer RCP. Currently, RCP replacement between 0 % and 30 % enhances compressive strength in alkali-activated materials. Huo et al. [22] found that samples with 50 % RCFP had a 28-day compressive strength of 59.05 MPa. Liu et al. [23] showed that replacing up to 50 % of GGBFS with RCP in geopolymer maintained good strength, but 100 % replacement significantly reduced strength. Studies confirm that RCP replacement below 30 % improves strength, but beyond 50 %, strength declines. However, factors influencing compressive strength of high-volume RCP alkali-activated slag remain unclear. The factors influencing the strength development of high-volume RCP alkali-activated slag systems remain insufficiently understood [24,25]. However, previous studies have indicated that the impact of increasing RCP replacement levels on compressive strength is governed by complex multi-factor interactions. In particular, synergistic effects between RCP fineness, mix design parameters, and activator composition may play a critical role in determining strength performance under high replacement conditions.

Therefore, to reveal the specific factors influencing the compressive strength of high-volume RCP-based alkali-activated slag mortar (HRAASM), this study builds upon the research of [22,23], using RCP to replace 60 % of GGBFS, with NaOH and Na_2SiO_3 as activators and river sand as fine aggregate. The response surface method (RSM) is utilized to design optimal mixture of HRAASM mortar, studying the degree of

Table 2
Particle size and specific surface area of RCP and GGBFS.

Materials	Particle size (μm)	Specific surface area (m^2/kg)
RCP−1	15.2	1510
RCP−2	24.4	1325
RCP−3	33.6	1309
GGBFS	10.57	1266

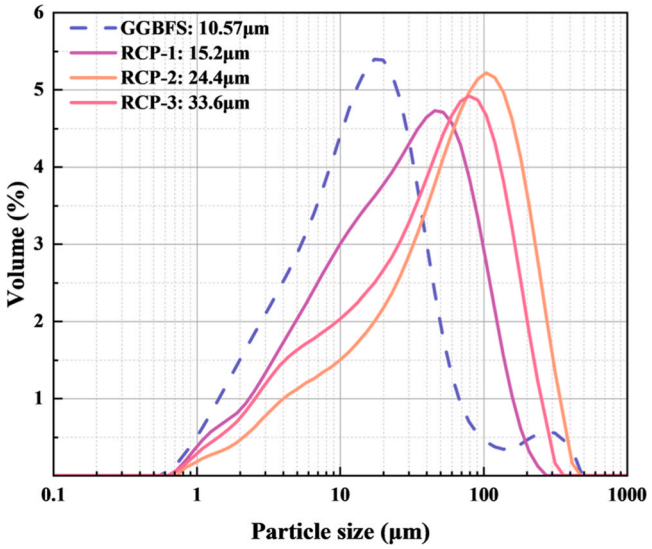

Fig. 2. The particle size distribution of RCP-1, RCP-2, RCP-3 and GGBFS.

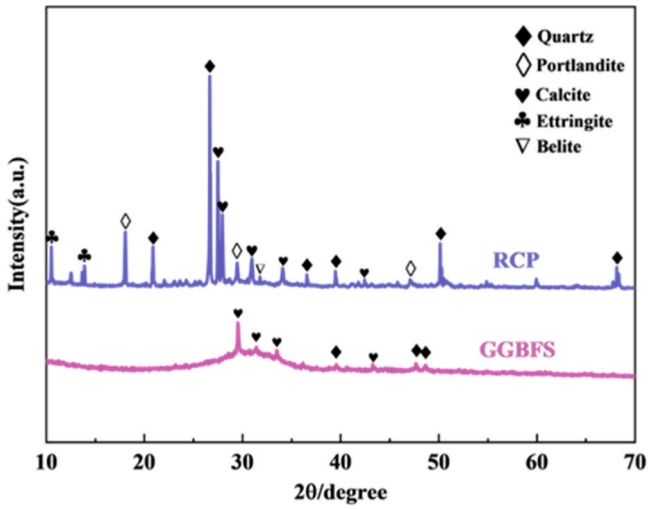

Fig. 3. XRD patterns of RCP and GGBFS.

Table 3
Experimental parameters and levels of variables for RSM.

Factors	Unit	Levels		
		Low (-1)	Center (0)	High (1)
A: RCP particle size	μm	15.2	24.4	33.6
B: Silica modulus (Ms)	-	1.2	1.4	1.6
C: Activator content	%	6	7	8
D: Water to solid ratio	-	0.46	0.48	0.5

influence of multi-factor interactions on the compressive strength of HRAASM. Then, X-ray diffraction (XRD), Fourier transform infrared spectroscopy (FTIR), thermogravimetric-differential scanning calorimetry (TG-DSC), and scanning electron microscopy (SEM) are employed to analyze the types and changes of reaction products in HRAASM, the degree of reaction, and the influence of the uniformity of reaction products on compressive strength, thus providing a better explanation for the changes of compressive strength. This research provides valuable insights into the high-volume use of RCP in AAS, particularly through the optimization of mix design parameters to achieve a high replacement ratio of RCP, which not only improves the compressive strength of AASM but also promotes the development of sustainable materials.

Table 4
The result of Box-Behnken design experiments.

Serial number	RCP particle size (μm)	Silica modulus (Ms)	Activator content (%)	Water to solid ratio	Compressive strength (MPa)
RMAW−1	24.4	1.4	7	0.48	53.5
RMAW−2	15.2	1.4	6	0.48	47.8
RMAW−3	33.6	1.6	7	0.48	57.5
RMAW−4	33.6	1.4	8	0.48	53.3
RMAW−5	15.2	1.4	7	0.46	52.5
RMAW−6	15.2	1.2	7	0.48	50
RMAW−7	24.4	1.4	6	0.5	44.5
RMAW−8	24.4	1.6	7	0.46	49.3
RMAW−9	33.6	1.4	6	0.48	45.9
RMAW−10	15.2	1.4	7	0.5	53.1
RMAW−11	15.2	1.4	8	0.48	50.7
RMAW−12	24.4	1.4	8	0.46	50.8
RMAW−13	24.4	1.4	7	0.48	54.4
RMAW−14	24.4	1.4	8	0.5	51.5
RMAW−15	24.4	1.4	7	0.48	53.6
RMAW−16	24.4	1.2	8	0.48	43.7
RMAW−17	33.6	1.2	7	0.48	39.6
RMAW−18	24.4	1.4	7	0.48	55.1
RMAW−19	24.4	1.2	7	0.46	44.7
RMAW−20	33.6	1.4	7	0.46	50
RMAW−21	24.4	1.4	7	0.48	53.7
RMAW−22	15.2	1.6	7	0.48	50.3
RMAW−23	24.4	1.6	7	0.5	52.9
RMAW−24	24.4	1.6	8	0.48	53.1
RMAW−25	33.6	1.4	7	0.5	49.3
RMAW−26	24.4	1.2	7	0.5	38.9
RMAW−27	24.4	1.6	6	0.48	49.4
RMAW−28	24.4	1.4	6	0.46	41.4
RMAW−29	24.4	1.2	6	0.48	36.8

2. Materials and methodology

2.1. Materials

GGBFS and RCP are utilized as binders in the formulation of HRAASM. Standard river sand, serving as the fine aggregate, is incorporated into these materials. GGBFS is sourced from Platinum run Refractory Co., Ltd. (Henan Province, China). The RCP used in this study originates from road demolition waste concrete that is over 10 years old and is crushed into fine powder with the particle size of below 0.15 mm. Fig. 1. portrays the appearance and particle morphology of RCP and GGBFS. Table 1 lists chemical compositions of RCP and GGBFS determined by Panalytical Axios X-ray fluorescence spectrometer. Table 2 presents the specific surface area of RCP and GGBFS with different particle sizes, measured by the Micromeritics ASAP 2460 automatic surface area and porosity analyser. Fig. 2. demonstrates the particle size distribution of RCP and GGBFS, gauged by the Malvern Mastersizer 3000 laser particle size analyser. Fig. 3 provides the mineral phases of RCP and GGBFS, determined by XRD. The main mineral phases of RCP are quartz (SiO_2), calcite ($CaCO_3$), ettringite ($3CaO{\cdot}Al_2O_3{\cdot}3CaSO_4{\cdot}30{\sim}32H_2O$), and portlandite ($Ca(OH)_2$). The mineral phases of slag micro-powder mainly are calcite ($CaCO_3$) and quartz (SiO_2). The fineness modulus of standard river sand is 2.68, with an absorption rate of less than 2 %, and the aggregate to binder ratio is 3.

Na_2SiO_3 and NaOH alkaline activators sourced from Henan Gongyi Borun Refractory Materials and Tianjin Ke Mao Limited Liability, respectively, are utilised for the production of alkali activated mortar. Na_2SiO_3 has a purity greater than 98.5 %, with a SiO_2 content of 54.1 % and Na_2O content of 24.2 % (SiO_2/Na_2O = 2.3). NaOH has a purity greater than 96 %.

2.2. Experimental design and mix proportion

RSM is utilized to systematically optimize the interactions among four key factors affecting mechanical performance of alkali-activated slag mortar (Table 3): RCP particle size, activator modulus (Ms),

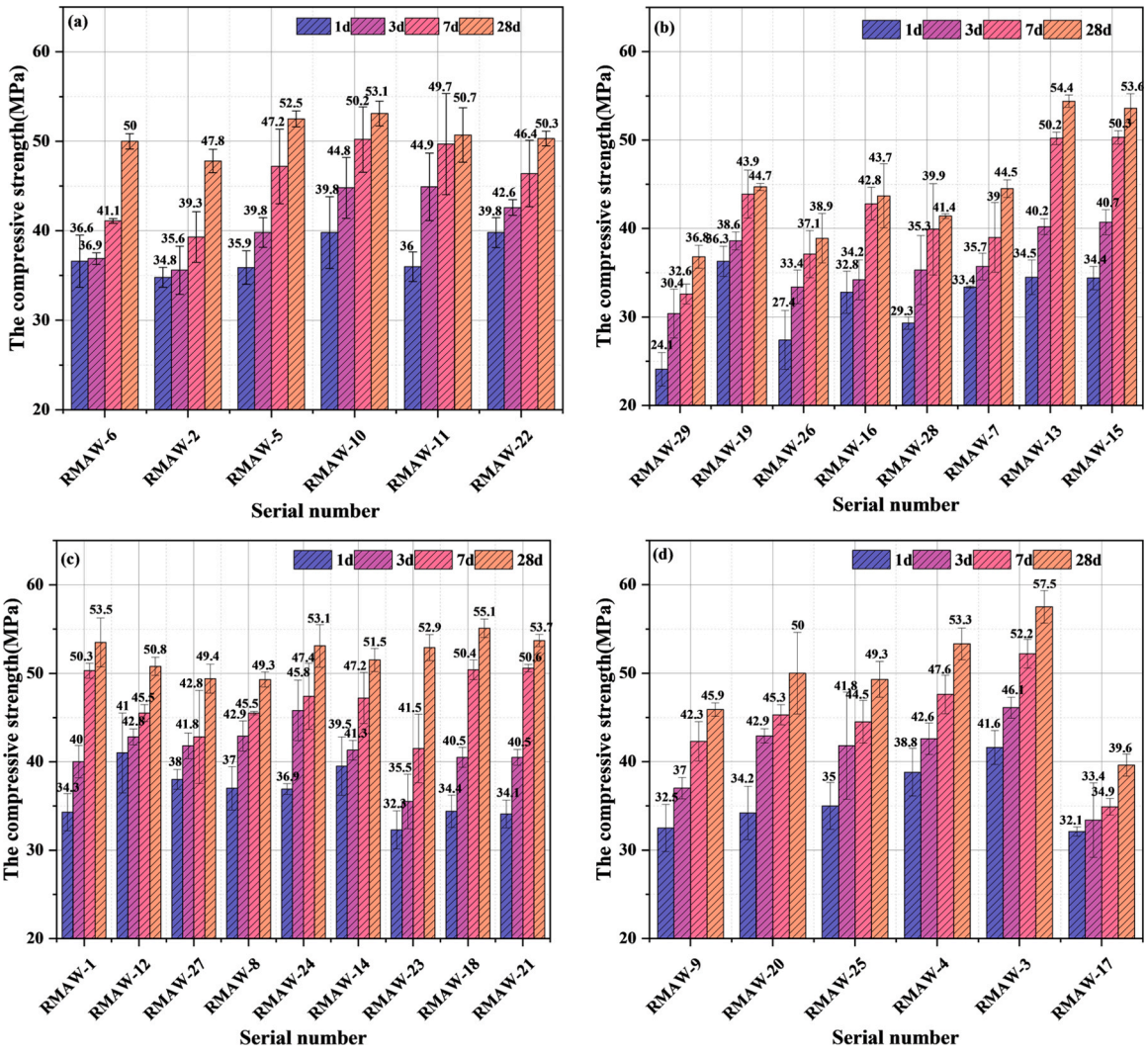

Fig. 4. Compressive strength curves of HRAASM containing RCP with different particle sizes: (a) RCP particle size: 15.2 μm, (b) and (c) RCP particle size: 24.4 μm, (d) RCP particle size: 33.6 μm.

activator content, and water-to-solid ratio (W/S). Table 4 uses a four-factor three-level Box-Behnken Design (BBD) to design the experiments with Design Expert 13 software, generating 29 experimental runs (including 24 factor/edge points and 5 center points for error estimation) to minimize the experimental workload while capturing quadratic relationships [26]. Compressive strength at 28 days is selected as the response variable. A quadratic polynomial model (Eq. 1) is fitted to predict the interactions between the factors [27,28], and its significance is verified through Analysis of Variance (ANOVA). This method ensures reliable optimization results while balancing cost-effectiveness and

Table 5
Variance analysis results of 28-day compressive strength model of HRAASM.

Source	Sum of Squares	Mean Square	F-value	P-value
Model	749.64	53.55	34.17	< 0.0001
A-RCP particle size (D50)	6.45	6.45	4.12	0.0619
B-silica modulus (Ms)	288.12	288.12	183.84	< 0.0001
C-Activator content	115.94	115.94	73.98	< 0.0001
D-Water to solid ratio	0.1875	0.1875	0.1196	0.7346
AB	77.44	77.44	49.41	< 0.0001
AC	5.06	5.06	3.23	0.0939
AD	0.4225	0.4225	0.2696	0.6117
BC	2.56	2.56	1.63	0.2220
BD	22.09	22.09	14.09	0.0021
CD	1.44	1.44	0.9188	0.3540
A^2	0.3685	0.3685	0.2351	0.6353
B^2	192.22	192.22	82.45	< 0.0001
C^2	110.42	110.42	70.45	< 0.0001
D^2	53.65	53.65	34.23	< 0.0001
Lack of Fit	20.09	2.01	4.34	0.0850

Table 6
Model accuracy result.

Model	Mean	C.V.%	R^2	Adjusted R^2	Predicted R^2	Adep Precision
28-day compressive strength	49.22	2.54	0.9716	0.9431	0.8463	23.6158

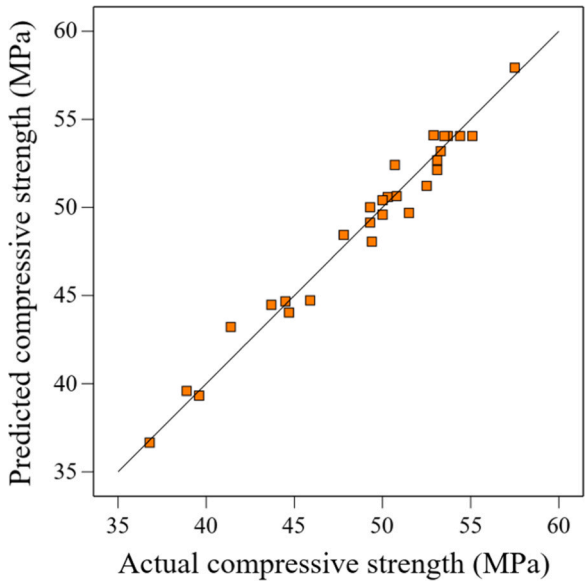

Fig. 5. Actual value and predicted value of the model.

robustness, avoiding extreme corner points in the variable space.

$$Y = \beta_0 + \sum_{i=1}^{4}\beta_i X_i + \sum_{i=1}^{4}\beta ii X_i^2 \sum_{i=1}^{4}\sum_{hj=1}^{4}\beta_{ij} X_i X_j \quad (1)$$

where Y denotes dependent variable, β_0 denotes constant coefficient, β_i denotes the coefficient of the linear effects, β_{ii} indicates the coefficient of quadratic effects, β_{ij} signifies the coefficient of the interaction effects, and X_i and X_j denote coded independent parameters.

In Table 4, taking RMAW-1 as an example, R indicates an RCP particle size, M represents a modulus of activator, A indicates an activator content, and W stands for a W/S. The rest of the numbering follows this pattern. The modulus of activator (Ms) is defined as the molar ratio of SiO_2 to Na_2O in the sodium silicate (Na_2SiO_3) and sodium hydroxide (NaOH) mixture. It is calculated using the formula Ms = (SiO_2) / (Na_2O), where SiO_2 and Na_2O denote the moles of silica and sodium oxide in the activator, respectively. The activator content refers to the mass ratio of Na_2O to the binder. The W/S ratio is defined as the mass ratio of total water (including activator solution and added water) to binders. The solid includes only the binders and does not include aggregates.

In the 24 h prior to mixing, solid granular NaOH and solid powdered Na_2SiO_3 were dissolved in 21.7 % water according to the specified proportions to prepare the alkali activator solution. Following the mix design proportions displayed in Table 4, the required amounts of precursor materials and river sand were weighed in accordance with Specification for mix proportion design of masonry mortar (JGJT98-2011) [29]. The weighed materials were placed in a drying oven at 65°C for 24 h to remove free water. Next, the solid powders, including slag powder and recycled concrete powder, were placed in a UJZ-15 vertical mortar mixer and mixed for 20 s. Purified water was then added (excluding the water mass in the activator solution), followed by the cooled activator solution, which was added to the paste and mixed again for 120 s. Eventually, the dried sand was added and mixed for another 120 s. The mix process was then completed. The mixed mortar was poured into 70.7 mm × 70.7 mm × 70.7 mm cube moulds, and mechanical vibration was applied to ensure compaction. After mixing, the mortar was allowed to sit in an environment with a temperature of 20 ± 5℃ for 24 ± 2 h before being numbered and demoulded. Immediately after demoulding, the samples were placed in an environment with the temperature of 20 ± 2℃ and the relative humidity of over 90 % for curing.

Using the same mix proportions and without adding river sand, NJ-160 cement paste was mixed to prepare cubes measuring 40 mm × 40 mm × 40 mm. These cubes were cured under the aforementioned conditions for a duration of 28 days for microscopic characterization testing.

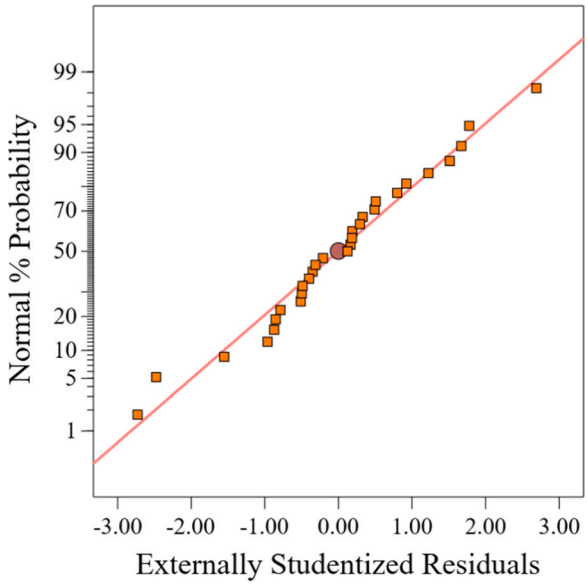

Fig. 6. Normal probability distribution of model residuals.

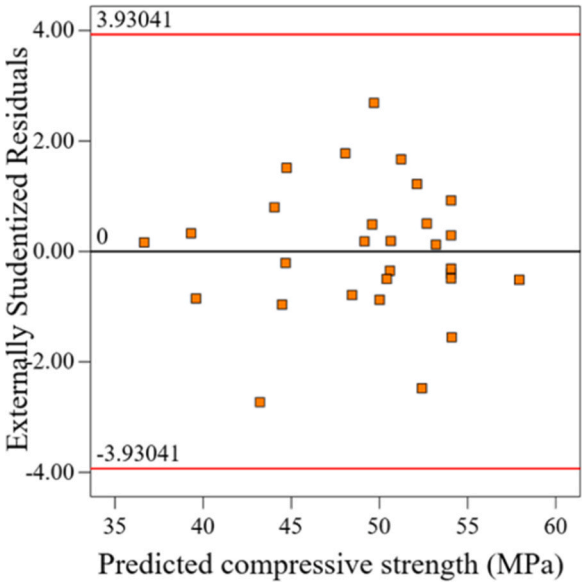

Fig. 7. Distribution of model residuals and predicted values.

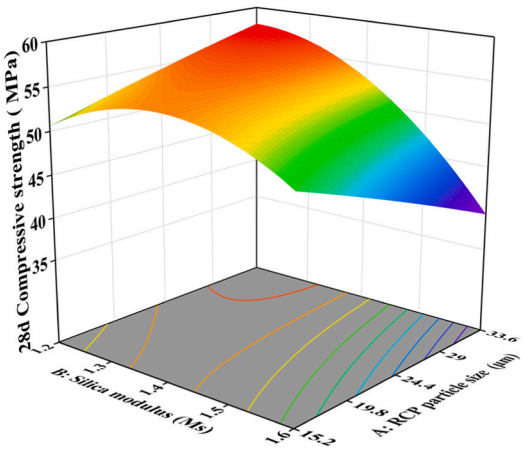

(a) Response of RCP particle size and Silica modulus (Ms).

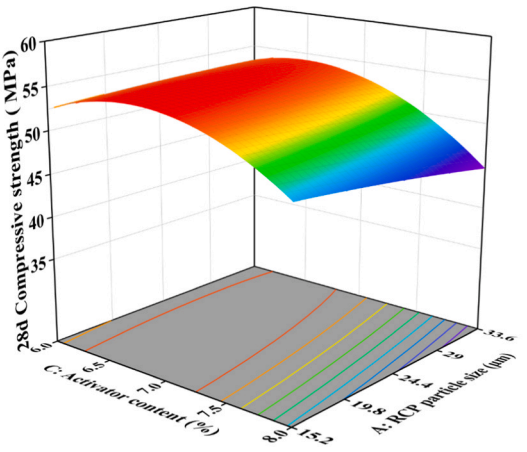

(b) Response of RCP particle size and Activator content.

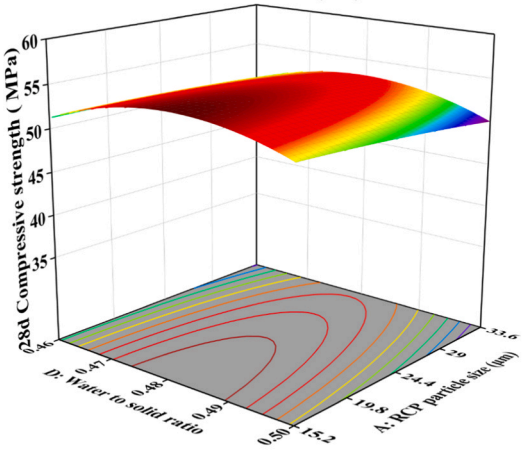

(c) Response of RCP particle size and W/S.

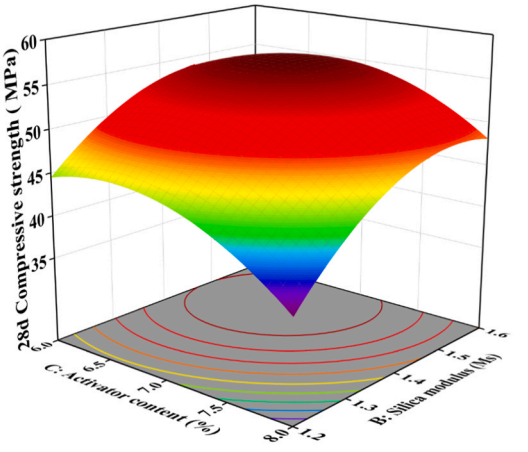

(d) Response of Silica modulus (Ms) and Activator content.

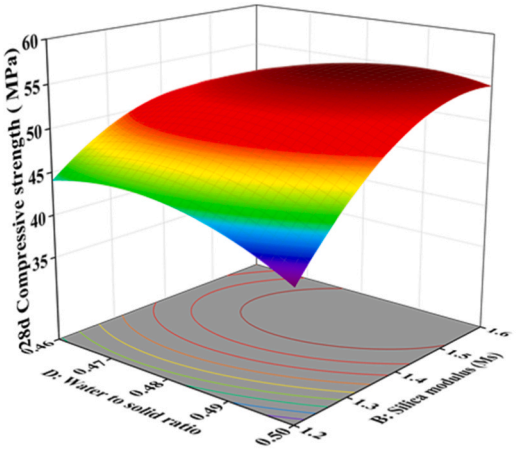

(e) Response of Silica modulus (Ms) and W/S.

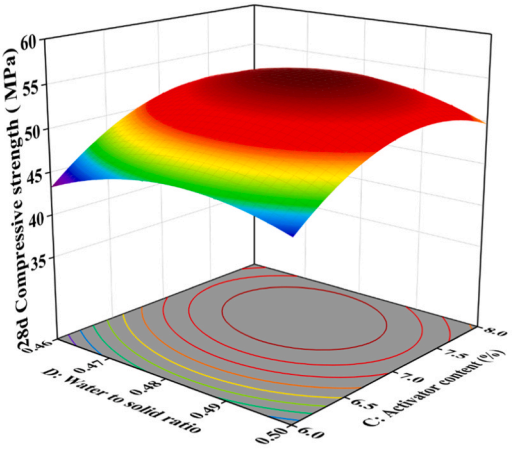

(f) Response of Activator content and W/S.

Fig. 8. The response of interaction of two factors to the 28-day compressive strength of HRAASM.

2.3. Test approaches

2.3.1. Compression test

According to Chinese standard JGJ/T 70-2009 [30] for cube compressive strength testing, the YAW-300 fully automatic pressure test machine was selected, with the loading speed of 1.5 KN/s. Cube specimens cured for 1, 3, 7, and 28 days were tested. The reported values of compressive strength were the average of three specimens, accurate to 0.1 MPa.

2.3.2. Micro-characteristics determination

Mineral analysis of samples was conducted using XRD. A 10 mg solid paste sample was immersed in isopropanol for one week and then dried at low temperature (50°C) for 24 h. The dried solid sample was ground into powder and placed on the sample holder. The Rigaku Ultima IV instrument was started, followed by self-check and calibration. The instrument settings were as follows: Cu-Kα radiation, wavelength: 1.5418 Å, voltage: 40 kV, current: 40 mA, scanning angle range: 5° to 80° 2θ, step size: 0.02° 2θ, and scanning speed: 5°/min.

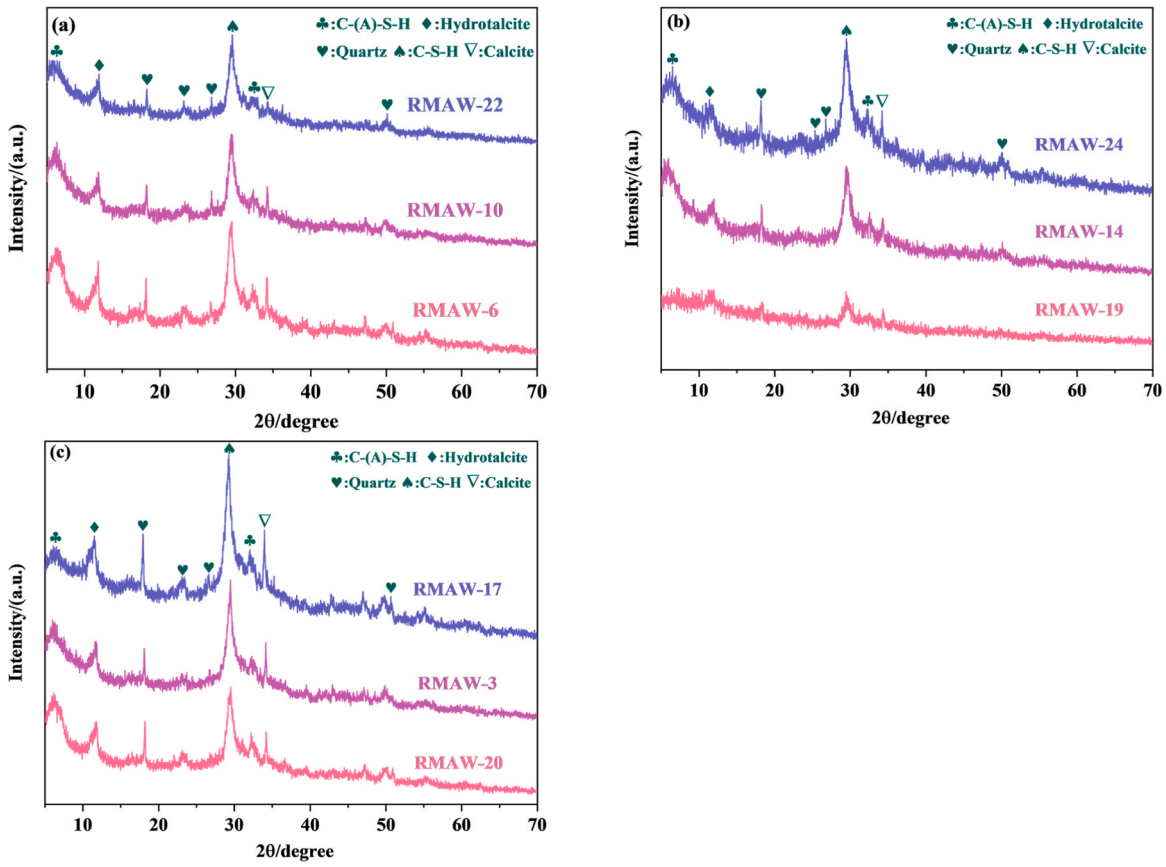

Fig. 9. XRD patterns of HRAASM incorporating RCP with different particle sizes: (a) RCP-1 particle size of 15.2 μm, (b) RCP-2 particle size of 24.4 μm, (c) RCP-3 particle size of 33.6 μm.

The FTIR spectra of the samples were collected using Fourier-transform infrared spectrometer (Thermo Scientific Nicolet iS20, USA), showing the absorption intensity at different wavelengths. In a dry environment, 10 mg of the sample, which had been soaked in isopropanol and dried at a low temperature (50°C) for 24 h, was mixed with a proper amount of dried potassium bromide (KBr) powder in a mortar and ground thoroughly several times. The mixture was subsequently placed into a pellet press and pressed into a transparent thin disc. During the test, the background spectrum was first collected, followed by the infrared spectrum of sample. The resolution was set to 4 cm^{-1}, with 32 scans performed, and the wavenumber was in the range of 400–4000 cm^{-1}.

TG-DSC tests were conducted using a simultaneous thermal analyser (Netzsch STA 449 F5, Germany). A powder sample weighing 10–20 mg was placed into a TG aluminium crucible. The sample was soaked in isopropanol to remove any excess solvent, then dried at a low temperature of 40°C-60°C, and stored in a desiccator to prevent moisture absorption. Under a nitrogen atmosphere, the sample was heated from 30°C to 1000°C at a specified heating rate of 10 °C/min.

The microstructure of the reaction products in the samples was obtained using ZEISS Gemini SEM 300 scanning electron microscope. A 10 mg bulk sample was soaked in isopropanol for one week and then dried at constant temperature of 50°C in a low-temperature oven for 24 h. The dried sample was directly adhered to conductive tape and sputter-coated with gold for 45 s utilizing a Quorum SC7620 sputter coater, with the sputtering current of 10 mA. Subsequently, the microstructure of the reaction products and elemental mapping were examined using the ZEISS Gemini SEM 300, with the accelerating voltage of 3 kV for morphological imaging, using the SE2 secondary electron detector.

3. Results and discussion

The 29 experimental samples are divided into four subgroups based on RCP particle size to analyze the main effect of particle size on mechanical performance and its interaction with activator parameters. Among them, the 7 samples with an RCP-1 particle size of 15.2 μm form one subgroup, the 15 samples with an RCP-2 particle size of 24.4 μm form another subgroup, and the 7 samples with an RCP-3 particle size of 33.6 μm form the third subgroup. By fixing the RCP particle size variable, the interaction effects are studied by adjusting other parameters (Ms, C, W/S). Compare the compressive strength values of different RCP particle sizes to identify the patterns of sensitivity to each parameter based on particle size.

3.1. *Effects of mix design parameters on compressive strength of HRAASM*

To analyze the interaction effects between RCP particle size and activator parameters, Fig. 4 divides the samples into three groups based on RCP particle size (15.2 μm, 24.4 μm, and 33.6 μm). Within each group, compressive strength curves under different combinations of activator modulus (Ms), activator content (C), and water to solid ratio (W/S) are shown to highlight the regulatory effect of particle size on parameter sensitivity. In Fig. 4(a), samples with an RCP-1 particle size of 15.2 μm show a consistent trend of high compressive strength. RMAW-22 (with the Ms of 1.6 and the W/S of 0.48) exhibits the highest compressive strength, indicating that higher silica modulus effectively enhances matrix strength, especially for smaller particle samples. The main reason is that smaller RCP particles can fill voids within the matrix more effectively [31–33]. Additionally, the active components in RCP, such as silicates and aluminates, are more easily dissolved and reacted at

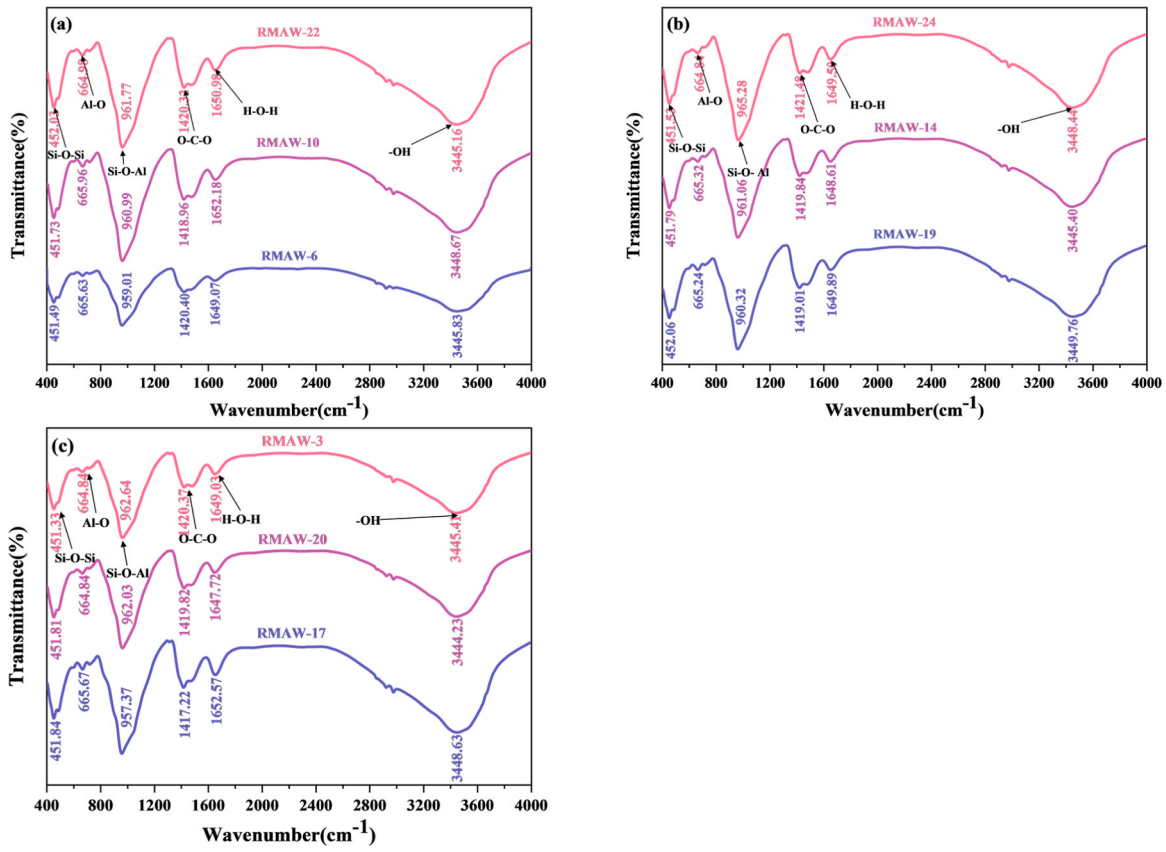

Fig. 10. FTIR curves of HRAASM containing RCP with different particle sizes: (a) RCP-1 particle size of 15.2 μm, (b) RCP-2 particle size of 24.4 μm, (c) RCP-3 particle size of 33.6 μm.

smaller particle sizes, forming more reaction products (C-S-H and C-A-S-H) [34,35], which are key to improving compressive strength of HRAASM samples. Conversely, the compressive strength of RMAW-6 (with a silica modulus of 1.2 and an activator content of 7 %) is lower than that of RMAW-1 (with a silica modulus of 1.4), further proving that raising silica modulus from 1.2 to 1.4 enhances matrix strength. Additionally, the RMAW-10 sample, which has a higher water to solid ratio (0.5), shows the lowest compressive strength in this group, indicating that smaller RCP particles are more sensitive to water content changes, and increasing the water to solid ratio significantly weakens their compressive performance.

For the samples in Fig. 4(b-c), with an RCP-2 particle size of 24.4 μm, the interaction between silica modulus, activator content, and water to solid ratio becomes more complex. Although this particle size still leads to relatively high compressive strength, it is slightly lower than that achieved by the 15.2 μm particles. The trend shows that as the RCP particle size increases, compressive strength tends to slightly decrease. For example, RMAW-12 (with silica modulus of 1.4 and activator content of 8 %) is the strongest in this group, indicating that an appropriate silica modulus and activator content can offset the strength reduction caused by larger particle sizes. Similarly, RMAW-27 performs well, showing that even for larger RCP particles, a higher silica modulus continues to enhance strength. In contrast, samples RMAW-26 and RMAW-23, both with the water to solid ratio of 0.5, exhibit significantly reduced strength, reinforcing the observation that higher water content negatively impacts compressive strength. When interacting with activator content, this excess water evaporates, leaving voids [36,37], especially for larger RCP particles, making the matrix more susceptible to strength loss related to water content.

For the samples in Fig. 4(d), with an RCP-3 particle size of 33.6 μm, compressive strength decreases further compared to smaller particle sizes. RMAW-3 exhibits the highest compressive strength in this group, indicating that a higher silica modulus can still improve matrix compressive strength by better binding slag particles [38,39], even with larger RCP particles. In contrast, RMAW-4 (with a silica modulus of 1.4 and an activator content of 8 %) shows lower strength, suggesting that too high an activator content may be detrimental to larger RCP particles. RMAW-1 (with the W/S of 0.46, and an activator content of 8 %) demonstrates one of the best performances, confirming that a lower water to solid ratio is critical for maintaining compressive strength, especially when using larger RCP particles.

Compared to previous studies on low RCP content, for example, Wang et al. [21] incorporated 10–30 % RCP into AAS mortar and evaluated the effect of RCP substitution levels on compressive strength. The activator modulus and alkali content for all samples were 1.8 and 8 %, respectively. At substitution rates of 10 %, 20 %, and 30 %, the compressive strengths of the AAS mortar at 28 days were 48 MPa, 45 MPa, and 42 MPa, respectively. In comparison, in this study, when the RCP substitution rate is 60 % and the alkali content is 8 %, changing the activator modulus to 1.2, 1.4, and 1.6 results in corresponding 28-day compressive strengths of 43.7 MPa, 50.3 MPa, and 53.1 MPa. This shows that when using high RCP content, an activator modulus of 1.6 is more beneficial for improving the matrix strength. At the same time, Wang et al. [33] used chemical activation to prepare alkali-activated recycled concrete powder cement (AARCPC). With an activator modulus of 1.4 and an alkali content of 6 %, they used 60 % RCP and 40 % slag, achieving a 28-day compressive strength of 45 MPa. In comparison, in this study, with the same activator modulus of 1.4 and alkali content of 6 %, when the RCP particle sizes are 15.2 μm, 24.4 μm, and 33.6 μm, the compressive strengths of the specimens are 47.8 MPa, 41.4 MPa, and 45.9 MPa, respectively. This indicates that changing the RCP particle size significantly alters the strength. In conclusion,

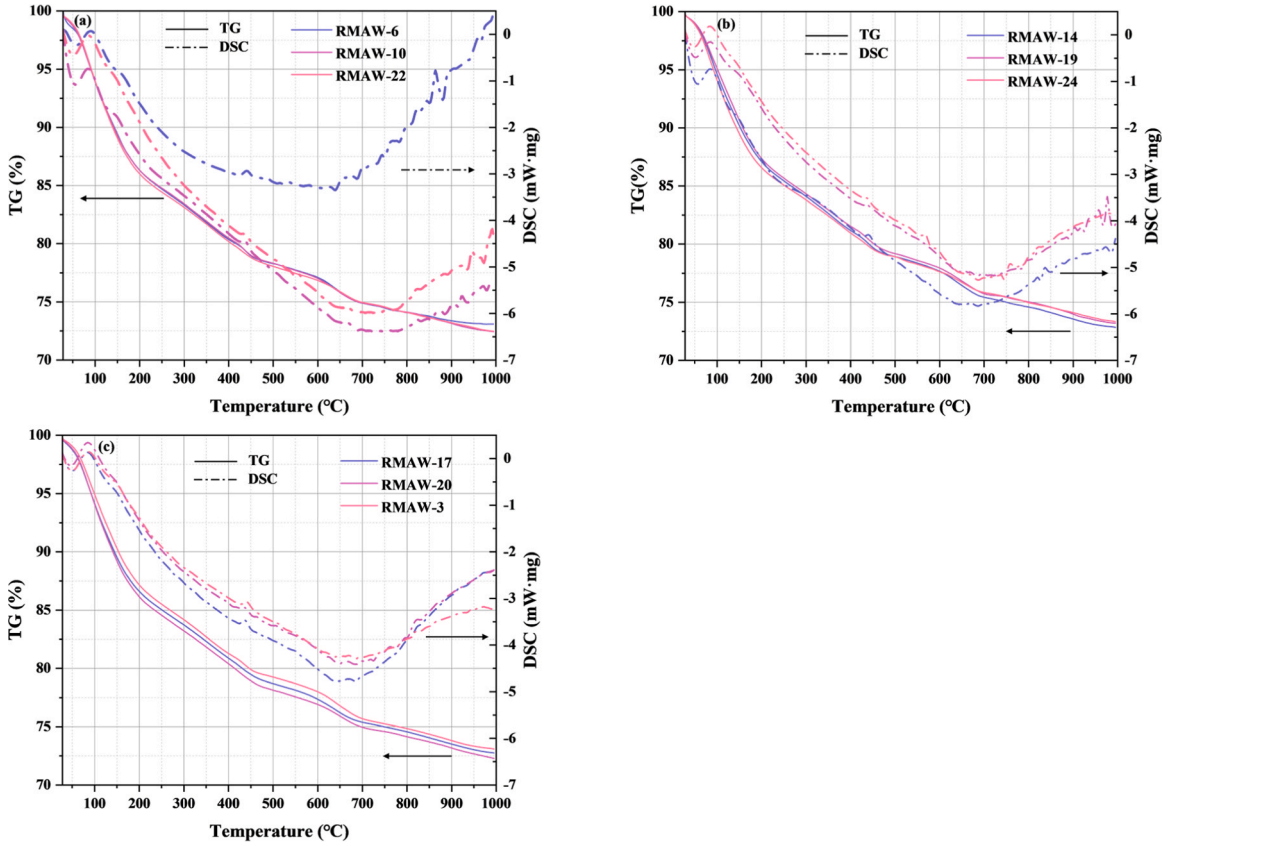

Fig. 11. TG-DSC curves of HRAASM containing RCP with different particle sizes: RCP-1 particle size (15μm): (a) RMAW-6, (b) RMAW-10, (c) RMAW-22; RCP-2 particle size (24.4μm): (d) RMAW-14, (e) RMAW-19, (f) RMAW-24; RCP-3 particle size (33.6μm): (g) RMAW-17, (h) RMAW-20, (i) RMAW-3.

compared to low RCP content studies, high RCP content is more sensitive to mix design parameters, and greater attention should be paid to the interaction of multiple factors in influencing its compressive strength.

This indicates that the complex interaction between multiple design parameters significantly affects the sample strength. In this context, RSM can systematically evaluate the interaction of these factors through the establishment of precise mathematical models, providing scientific guidance for optimizing mix design to ensure effective improvement in matrix compressive strength.

3.2. Model establishment and variance analysis

Using RCP particle size (A), silica modulus (Ms) (B), activator content (C), and W/S (D) as independent variables, and 28-day compressive strength of 29 groups of HRAASM in Fig. 6 as the evaluation index, a multivariate regression model is fitted and optimized, resulting in the response Eq. (2) and the corresponding fitted regression model.

$$Y_{28d} = 54.06 - 0.7333A + 4.9B + 3.11C + 0.125D + 4.4AB + 1.12AC - 0.325AD - 0.8BC + 2.35BD - 0.6CD - 0.2383A^2 - 4.46B^2 - 4.13C^2 - 2.88D^2 \quad (2)$$

The analysis of variance of the simulation equation can assess the accuracy and robustness of the model. The variance analysis results for 28-day compressive strength regression model of HRAASM are shown in Table 5. In statistical significance testing methods, the P-value can be used for hypothesis testing and mismatch testing analysis. The P-value below 0.01 reveals a highly substantial difference between samples, the P-value ranging from 0.01 to 0.05 is deemed significant, and the P-value higher than 0.05 is considered not significant. It is observed that the P-value of model established is below 0.0001, which has a highly significant impact on the results, and the lack of fit is higher than 0.05, which is not significant, indicating high reliability of the model. A P-value below 0.05 reveals that significance for model terms. In this case, B, C, AB, BD, B^2, C^2, and D^2 are identified as significant terms. Table 6 presents model's fitting accuracy, showing that the difference between the adjusted correlation coefficient (Adj R^2) and the predicted correlation coefficient (Pred R^2) is below 0.2, indicating an excellent fit for the regression model. The signal-to-noise ratio (S/N) is higher than 4, showing good accuracy of model. Fig. 5 compares the real and predicted values of model, showing that these values are distributed along or on both sides of the y = x line, indicating a good match between the experimental results and theoretical predictions. Fig. 6 displays normal probability distribution of model residuals, which closely aligns with a straight line. Fig. 7 shows the distribution of the model residuals and predicted values, which is irregular. These results indicate that the model based on 28-day compressive strength of HRAASM is able to effectively reflect the changing pattern of HRAASM compressive strength with various factors.

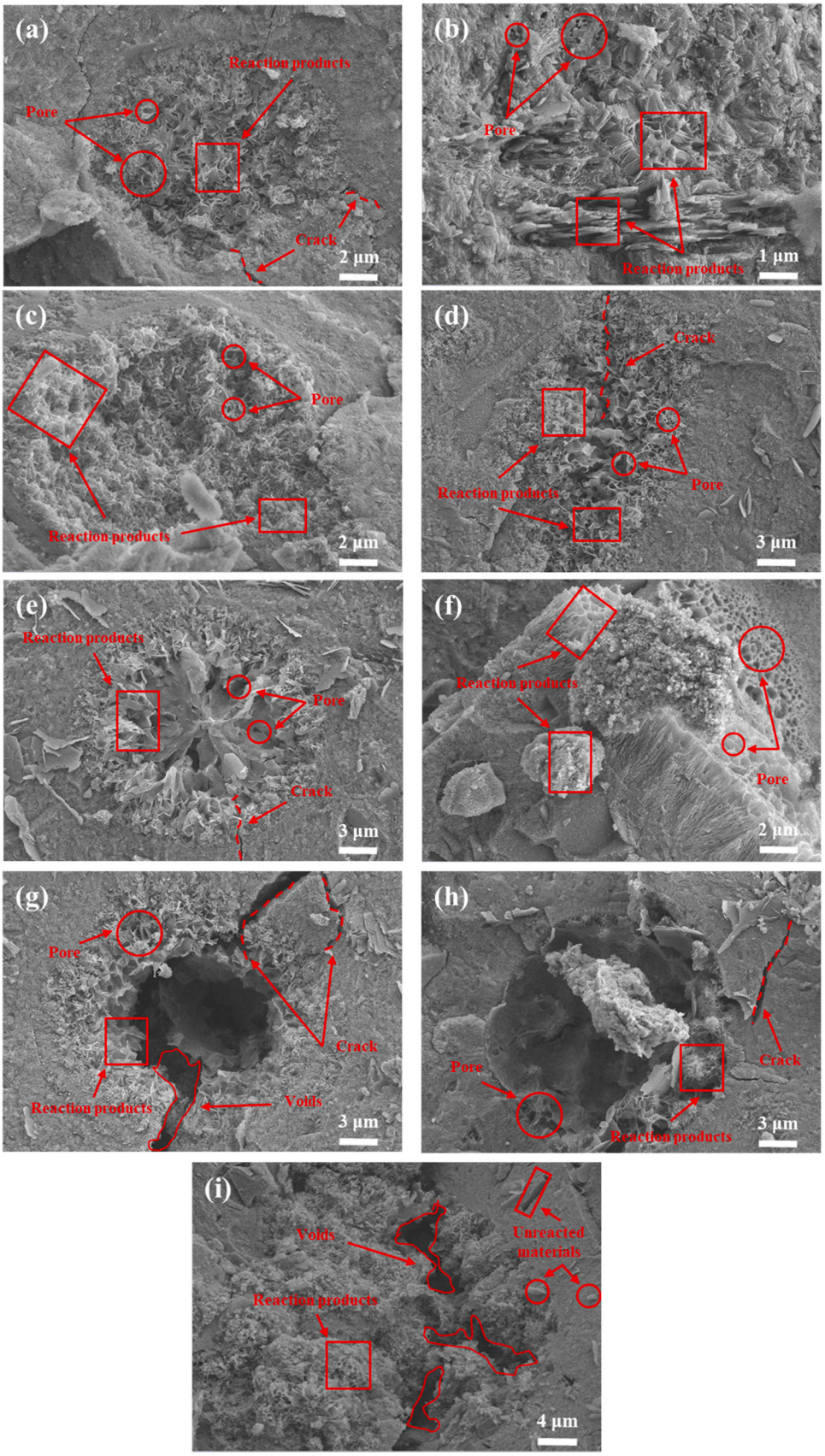

Fig. 12. SEM Images of Matrix Uniformity of HRAASM: (a) RMAW-6, (b) RMAW-10, (c) RMAW-22, (d) RMAW-19, (e) RMAW-14, (f) RMAW-24, (g) RMAW-20, (h) RMAW-3, (i) RMAW-17.

3.3. Response surface analysis

Fig. 8 shows the interaction between RCP particle size (D50) (A), silica modulus (Ms) (B), activator content (C), and W/S (D) on compressive strength. It indicates that combining activator content and silica modulus has the greatest influence on compressive strength, especially when the silica modulus is high, where an increase in activator content significantly enhances compressive strength. The combination of smaller RCP particle size and higher activator content also shows the best effect, while increasing W/S ratio tends to weaken the positive effects of other factors. Overall, the order of effects of individual factors on compressive strength is activator content (C) > silica modulus (B) > RCP particle size (A) > water to solid ratio (D). The order of interaction between two factors is BC > AB > CD > BD > AC > AD.

3.4. Microstructure of sample

Although response surface analysis reveals the interaction effects between different mix design parameters and provides quantitative trends, it is limited in its ability to explain the underlying reasons for these trends. Therefore, it is necessary to conduct characterization tests to further study internal microstructure and composition of the samples and explain fundamental reasons behind the changes in compressive strength from a mechanistic perspective. In this study, samples are divided into three groups based on RCP particle size: 15.2μm, 24.4μm, and 33.6μm. According to the response surface analysis, the key factors influencing compressive strength are B, C, AB, and BD. Based on this, three samples are selected from each group for characterization: the samples from the first group (15.2μm) are RMAW-6, RMAW-10, and RMAW-22; the samples from the second group (24.4μm) are RMAW-14, RMAW-19, and RMAW-24; the samples from the third group (33.6μm) are RMAW-3, RMAW-17, and RMAW-20, totalling nine samples. These samples are characterized and analysed to explain how different compositions of RCP affect the formation of hydration products and how various mix design parameters influence the compressive strength of samples.

3.4.1. XRD analysis

Fig. 9 analyses XRD patterns of different HRAASM samples, exploring the effects of different mix design parameters on the formation of reaction products and compressive strength. Comparing original phases of two raw materials in Fig. 4, it is clear that some active phases in RCP and GGBFS (such as ettringite, calcium hydroxide, gypsum, belite) disappear because they are unstable in an alkali-activated environment, dissolving and releasing ions such as Ca^{2+}, Al^{3+}, and SiO_4^{2-} [34], which then participate in generating C-S-H or C-(A)-S-H gels, causing their disappearance after reaction. Other inert phases (such as calcite and quartz) persist, as their chemical properties are stable and they do not dissolve or react in the alkali-activated system, thus continuing to exist as inert phases in the system. As shown in Fig. 9, the amorphous humps between 5 and 7° 2θ and 28–30° 2θ correspond to C-(A)-S-H and C-S-H, with the intensity of the hump reflecting the amount of gel phase produced [40]. RMAW-3 and RMAW-24 exhibit significant amorphous humps, indicating that they generated a large amount of C-(A)-S-H and C-S-H. The higher silica modulus (such as 1.6) further promotes the formation of these gel phases, which corresponds to their higher compressive strength, especially for RMAW-3, which achieves a compressive strength of 57.5 MPa, suggesting that the formation of the amorphous phase effectively enhances the sample's density. In contrast, RMAW-17 and RMAW-19 show weaker amorphous humps, indicating insufficient reaction. A lower silica modulus (such as 1.2) results in less gel phase formation, leading to lower compressive strength (39.6 MPa and 44.7 MPa, respectively). Additionally, smaller RCP particle size (such as 15.2 μm) provides larger specific surface area and more reaction sites [41,42], which is capable of accelerating dissolution and reaction of active phases, further promoting the generation of amorphous phase (C-S-H and C-(A)-S-H), thereby improving compressive strength. Sharp diffraction peak between 11 and 12° 2θ corresponds to hydrotalcite [35]. Strong hydrotalcite peaks are observed in RMAW-22, RMAW-24, and RMAW-20, indicating that the increased activator content accelerates the reaction, promoting the formation of the amorphous phase and secondary phases (such as hydrotalcite) [20]. This enhanced reactivity contributes to forming denser matrix, as discussed further in Section 3.4.4. In contrast, hydrotalcite peaks with lower intensity are found in RMAW-6 and RMAW-19, where W/S and activator content jointly affect the reaction degree. Samples with a lower W/S (such as RMAW-19) show less hydrotalcite formation, possibly resulting in lower compressive strength. The sharp diffraction peaks at 17–18°, 22–23°, 26–27°, and 49–50° 2θ correspond to quartz [43], and quartz peaks are observed in all samples, indicating that the RCP includes a large amount of quartz particles. These quartz particles act as inert fillers [44,45], not participating in the alkali-activation reaction. This also indicates that RCP primarily contributes to early compressive strength development through a physical filling effect. However, larger RCP particles may not act purely as inert fillers, as they can influence pore structure refinement and potentially affect long-term durability and shrinkage behaviour. Therefore, their impact requires further quantitative evaluation through systematic durability and shrinkage tests. The sharp diffraction peak between 34 and 35° 2θ corresponds to calcite, and its content reflects the degree of reaction of RCP. Higher calcite peaks in RMAW-20 and RMAW-10 indicate that a larger amount of unreacted calcium carbonate remains in these samples, potentially reducing reactivity [46], thereby affecting compressive strength. In contrast, RMAW-3 and RMAW-24 show lower calcite peaks, suggesting that the reactive components in RCP (such as Al_2O_3 and CaO) are more fully involved in reaction.

3.4.2. FTIR analysis

Fig. 10 portrays FTIR spectra of HRAASM samples with different mix design parameters. First, the vibration peaks of O-Si-O, Si-O-Si, and Si-O-T at 451–965 cm^{-1} in the FTIR correspond to the amorphous phase humps at 5–7° and 28–30° in the XRD [47–49], indicating the generation of C-S-H and C-(A)-S-H gel phases [50]. Higher silica modulus (e.g., 1.6) and smaller RCP particle size (e.g., 15.2 μm) promote the generation of these gel phases, as reflected in the high strength of 57.5 MPa in the RMAW-3 sample. Second, the Al-O stretching peak at 664 cm^{-1} in FTIR corresponds to hydrotalcite peak at 11–12° in the XRD [51,52], showing that enhanced aluminium-based reactions improve the stability of the gel phase, especially in the RMAW-24 sample, where the higher activator content promotes the formation of hydrotalcite [38], strengthening the compressive strength. Additionally, the CO_3^{2-} stretching peak around 1417 cm^{-1} and the calcite peak at 34–35° in the XRD show that residual calcite in RCP did not participate in the reaction [53]. The higher calcite content in RMAW-20 and RMAW-19 reduces reactivity, affecting compressive strength [54]. Finally, the H-O-H and -OH vibration peaks at 1647–3449 cm^{-1} reflect the presence of structural water [55]. Excess structural water hinders the formation of gel phases [56], as confirmed by the lower amorphous phases shown by XRD data, further explaining the lower compressive strength in RMAW-17 and RMAW-19.

3.4.3. TG-DSC analyses

Fig. 11 analyses the mass loss and endothermic peaks of HRAASM samples at different temperatures through TG-DSC. In the low-temperature range (30°C-200°C), the mass loss shown in TG curve is primarily associated with the evaporation of structural water in the C-S-H and C-(A)-S-H gel phases [20,57,58]. Smaller RCP particle sizes (such as 15.2 μm and 24.4 μm) provide more reaction sites [18], promoting the generation of C-S-H and C-(A)-S-H gel phases. This is reflected in greater mass loss and more pronounced DSC endothermic peaks in samples with higher silica modulus, such as RMAW-3 and RMAW-10 (1.6 and 1.4). This indicates that the combination of smaller RCP particle size and

higher silica modulus promotes the formation of more gel phases, allowing water to evaporate more easily and absorb a large amount of heat. In contrast, samples with larger RCP particle sizes (such as 33.6 μm), like RMAW-17, exhibit reduced reaction sites and lower silica modulus (1.2), resulting in less gel formation, and consequently, weaker mass loss and endothermic peaks in the low-temperature range, reflecting lower water content and insufficient reaction, which affects the improvement of compressive strength. In medium temperature range (200°C-400°C), the mass loss in TG curve is mainly associated with the dehydration decomposition of hydrotalcite [20,21,59]. Higher silica modulus (as in RMAW-3 and RMAW-22) and appropriate activator content promote the formation of hydrotalcite, with the TG curve showing significant mass loss, corresponding to the hydrotalcite formation observed in the XRD images. Simultaneously, the DSC curve also shows obvious endothermic peaks in this range, indicating that the dehydration process of hydrotalcite absorbs a large amount of heat, reflecting the stability of the internal structure of the matrix. In contrast, samples like RMAW-19 and RMAW-17 with lower silica modulus show less mass loss and weaker endothermic peaks in this temperature range, indicating less hydrotalcite formation and relatively lower compressive strength. In the high-temperature range (400°C-800°C), the mass loss in the TG curve is primarily associated with the decomposition of calcite [60,61]. RMAW-20 and RMAW-19, with higher calcium carbonate content, exhibit greater mass loss in this temperature range, and the DSC curve shows significant exothermic peaks, reflecting the release of a large amount of heat during calcite decomposition. This indicates that there is a higher amount of unreacted calcium carbonate in these samples, which has not fully participated in the alkali activation reaction. As the temperature rises, the degree of calcium carbonate decomposition increases, resulting in greater mass loss in the TG curve and stronger exothermic peaks in the DSC curve.

3.4.4. Analysis of microstructure and matrix uniformity

Fig. 12 shows the SEM images of the samples, where key features such as pores, cracks, and reaction products in the matrix are highlighted. Observing Fig. 12(a-c), samples with smaller RCP particles (15.2 μm), such as RMAW-6, RMAW-10, and RMAW-22, show more uniform reaction products, denser structures, and relatively fewer cracks. For example, RMAW-10 (Ms=1.4, W/S=0.5) exhibits finer pores and denser reaction products, leading to a high compressive strength of 53.1 MPa. A higher Ms and smaller particle size allow for more reaction sites [18,21], promoting the formation of C-S-H and C-(A)-S-H gels. Observing Fig. 12 (d-f), in samples with medium RCP particles (24.4 μm), such as RMAW-14, RMAW-19, and RMAW-24, the reaction products are still prominent, but larger pores and more noticeable cracks are visible. For instance, RMAW-19 (Ms=1.2, W/S=0.46) exhibits a more porous structure, leading to lower compressive strength of 44.7 MPa. The lower Ms and larger particle size lead to reduced uniformity in gel formation and increased porosity [62,63], consequently reducing the matrix strength. Fig. 12(g-i) also show that samples with larger RCP particles, such as RMAW-17, RMAW-20, and RMAW-3, display more prominent pores and cracks. RMAW-17, with a silica modulus of 1.2, exhibits less well-connected matrix with higher porosity and underdeveloped reaction products, leading to the lowest compressive strength of 39.6 MPa. Larger RCP particles reduce the surface area available for the alkali activation reaction [64,65], resulting in insufficient gel formation and reduced overall matrix integrity.

4. Conclusions

On basis of experimental results, the impacts of mixture parameters on microstructure and mechanical strength of HRAASM are evaluated, and the reaction products, reaction process, and microstructure of HRAASM are analysed. The detailed findings are drawn as follows:

(1) The RSM model effectively captures multi-parameter interactions, demonstrating high accuracy ($R^2 = 0.9716$) and reliability (S/N ratio > 4). The predicted compressive strength shows an average error of < 5 % compared to the experimental results, providing a reliable tool for mix design optimization of high-volume RCP-based alkali-activated materials.
(2) The alkali-activated slag mortar containing 60 % RCP exhibits viable mechanical performance, with the 28-day compressive strength range of 36.8–57.5 MPa. Optimal mix design is RCP particle size: 15.2 μm, silica modulus: 1.59, activator content: 7.42 %, and water to solid ratio: 0.47, which validates the potential of RCP as a sustainable precursor in high-performance alkali-activated slag systems. However, the impact of high RCP content on the long-term durability of the mortar remains unclear and still requires further investigation and validation through subsequent systematic experimental studies.
(3) RCP particles of 15.2 μm significantly enhance reactivity by providing a higher specific surface area, accelerating the dissolution of active components, and promoting the generation of amorphous gels. An activator modulus of 1.6 optimizes the alkali activation process, facilitating the formation of dense C-S-H/C-A-S-H networks, while a W/S of 0.46 minimizes capillary pores and microcracks.
(4) The analyses of XRD and SEM confirm that inert phases (quartz, calcite) act as fillers, while unreacted calcite causes mass loss at high temperatures. Excessive water content (W/S = 0.5) leads to pore coarsening, especially for larger RCP particles (33.6 μm), resulting in a 30–40 % reduction in compressive strength.

CRediT authorship contribution statement

Jiehong Li: Writing – review & editing, Validation. **Han Gao:** Writing – review & editing. **Yingda Zhang:** Writing – review & editing. **Yang Yu:** Writing – review & editing, Supervision, Project administration. **Chunwei Zhang:** Funding acquisition. **Zhen Zou:** Writing – original draft, Methodology, Formal analysis, Conceptualization. **Jingyun Li:** Software, Investigation, Data curation.

Declaration of Competing Interest

The authors declare that they have no known competing financial interests or personal relationships that could have appeared to influence the work reported in this paper.

Acknowledgements

This research is financially supported by the National Natural Science Foundation of China (Grant No. 52361135807), the Department of Science and Technology of Shandong Province (Grant No. 2021CXGC011204), and the Liaoning provincial key laboratory of Safety and Protection for Infrastructure Engineering.

Data availability

Data will be made available on request.

References

[1] Sharma P. A brief account of man, material and manufacturing: on the timeline. Mater Today Proc 2022;66:3572–7.
[2] Yonis A, Vashistha P, Oinam Y, Cyr M. Novel utilization of waste concrete powder in alkali-activated binder. J CO_2 Util 2024;84:102859.
[3] Vaverková MD, Maxianová A, Winkler J, Adamcová D, Podlasek A. Environmental consequences and the role of illegal waste dumps and their impact on land degradation. Land Use Pol 2019;89:104234.
[4] Li L, Liu Q, Huang T, Peng W. Mineralization and utilization of CO_2 in construction and demolition wastes recycling for building materials: a systematic review of

recycled concrete aggregate and recycled hardened cement powder. Sep Purif Technol 2022;298:121512.
[5] Chen H, Chow CL, Lau D. Developing green and sustainable concrete in integrating with different urban wastes. J Clean Prod 2022;368:133057.
[6] Tošić N, Marinković S, Dašić T, Stanić M. Multicriteria optimization of natural and recycled aggregate concrete for structural use. J Clean Prod 2015;87:766–76.
[7] Liu L, Li Z, Cai G, Zhang J, Dai B. Long-term performance of temperature and humidity in the road embankment constructed with recycled construction and demolition wastes. J Clean Prod 2022;356:131851.
[8] Huang J, Zou C, Sun D, Yang B, Yan J. Effect of recycled fine aggregates on alkali-activated slag concrete properties. Structures 2021;30:89–99.
[9] Mandal R, Panda SK, Nayak S, Chakraborty S. Efficacy of pond ash (PA) combined with ground granulated blast furnace slag (GGBFS) in producing cement-less mortar. Structures 2022;45:748–57.
[10] Zhang M, Zhu L, Gao S, Dong Y, Yuan H. Mechanical properties of recycled aggregate concrete prepared from waste concrete treated at high temperature. J Build Eng 2023;76:107045.
[11] Zhu P, Chen X, Liu H, Wang Z, Chen C, Li H. Recycling of waste recycled aggregate concrete in freeze-thaw environment and emergy analysis of concrete recycling system. J Build Eng 2024;96:110377.
[12] Al-Waked Q, Bai J, Kinuthia J, Davies P. Enhancement of mechanical properties of concrete with treated demolition waste aggregate. J Build Eng 2022;58:105047.
[13] Mohtasham Moein M, Rahmati K, Mohtasham Moein A, Rigby SE, Saradar A, Karakouzian M. Utilizing construction and demolition waste in concrete as a sustainable cement substitute: a comprehensive study on behavior under short-term dynamic and static loads via laboratory and numerical analysis. J Build Eng 2024;97:110778.
[14] Ruth Bola Oliveira D, Leite G, Possan E, Marques Filho J. Concrete powder waste as a substitution for Portland cement for environment-friendly cement production. Constr Build Mater 2023;397:132382.
[15] Wu H, Wang C, Ma Z. Drying shrinkage, mechanical and transport properties of sustainable mortar with both recycled aggregate and powder from concrete waste. J Build Eng 2022;49:104048.
[16] Ma Z, Shen J, Wu H, Zhang P. Properties and activation modification of eco-friendly cementitious materials incorporating high-volume hydrated cement powder from construction waste. Constr Build Mater 2022;316:125788.
[17] Liu X, Liang C, Zhang Z, Zhang Y, Xu J, Ma Z. Mechanical performance of low-carbon ultra-high performance engineered cementitious composites (UHP-ECC) with high-volume recycled concrete powder. J Build Eng 2024;88:109153.
[18] Wu H, Yang D, Wang C, Ma Z. Effects of construction waste powder on micro–macro properties of green high-strength cement paste with low water-to-binder ratio. Constr Build Mater 2023;385:131493.
[19] Ren P, Li B, Yu J, Ling T. Utilization of recycled concrete fines and powders to produce alkali-activated slag concrete blocks. J Clean Prod 2020;267:122115.
[20] Liang G, Liu T, Li H, Wu K. Shrinkage mitigation, strength enhancement and microstructure improvement of alkali-activated slag/fly ash binders by ultrafine waste concrete powder. Compos B Eng 2022;231:109570.
[21] Wang H, Wang L, Shen W, Cao K, Sun L, Wang P, Cui L. Compressive strength, hydration and pore structure of alkali-activated slag mortars integrating with recycled concrete powder as binders. KSCE J Civ Eng 2022;26:795–805.
[22] Huo W, Zhu Z, Sun H, Gao Q, Zhang J, Wan Y, Zhang C. Reaction kinetics, mechanical properties, and microstructure of nano-modified recycled concrete fine powder/slag based geopolymers. J Clean Prod 2022;372:133715.
[23] Liu M, Wang C, Wu H, Yang D, Ma Z. Reusing recycled powder as eco-friendly binder for sustainable GGBS-based geopolymer considering the effects of recycled powder type and replacement rate. J Clean Prod 2022;364:132656.
[24] Wang L, Yi S, Yu Y, Gao C, Samali B. Automated ultrasonic-based diagnosis of concrete compressive damage amidst temperature variations utilizing deep learning. Mech Syst Signal Pr 2024;221:111719.
[25] Yu Y, Rashidi M, Dorafshan S, Samali B, Farsangi EN, Yi S, Ding Z. Ground penetrating radar-based automated defect identification of bridge decks: A hybrid approach. J Civ Struct Health 2025;15:563–73.
[26] Gunst RF. Response surface methodology: process and product optimization using designed experiments. Technometrics 1996;38:284–6.
[27] Mousavi S, Gheibi M, Wacławek S, Smith NR, Hajiaghaei-Keshteli M, Behzadian K. Low-energy residential building optimisation for energy and comfort enhancement in semi-arid climate conditions. Energy Conv Manag 2023;291:117264.
[28] Li Y, Huang L, Gao C, Qu Y, Luo X, Lv B, Chen Z. Axial compressive behavior of steel reinforced GGBS-RFBP-FA ternary composite geopolymer recycled fireclay brick aggregates concrete columns. Structures 2024;60:105913.
[29] JGJ/T 98-2011. Specification for mix proportion design of masonry mortar. Beijing, China: China Architecture & Building Press; 2011.
[30] JGJ/T 70-2009. Ministry of Housing and Urban-Rural Construction of the People's Republic of China. Standard for Test Methods of basic properties of construction mortar. Beijing, China: China Architecture & Building Press; 2009.
[31] Chen K, Wu D, Zhang Z, Pan C, Shen X, Xia L, Zang J. Modeling and optimization of fly ash–slag-based geopolymer using response surface method and its application in soft soil stabilization. Constr Build Mater 2021;315:125723.
[32] Liu M, Wu H, Yao P, Wang C, Ma Z. Effect of ground concrete waste as green binder on the micro-macro properties of eco-friendly metakaolin-based geopolymer mortar. J Build Eng 2023;68:106191.
[33] Wang X, Yan Y, Tong X, Gong Y. Investigation of mineral admixtures on mechanical properties of alkali-activated recycled concrete powders cement. Buildings 2022;12:1234.
[34] Huo W, Zhu Z, Chen W, Zhang J, Kang Z, Pu S, Wan Y. Effect of synthesis parameters on the development of unconfined compressive strength of recycled waste concrete powder-based geopolymers. Constr Build Mater 2021;292:123264.
[35] Yao T, Tian Q, Zhang M, Qi S, Wang C, Ruan M. Laboratory investigation of foamed concrete prepared by recycled waste concrete powder and ground granulated blast furnace slag. J Clean Prod 2023;426:139095.
[36] Li J, Yu Q, Huang H, Yin S. Difference in the reaction process of slag activated by waterglass solution and NaOH solution. Struct Concr 2019;20:1528–40.
[37] Kong L, Fan Z, Lu J, Zhang L. Microstructure evolution of interfacial transition zone between alkali-activated fly ash/slag matrix and aggregate. Mater Struct 2022;55:203.
[38] Sasui S, Kim G, Nam J, Alam SF, Eu H, Lee Y, Ahmad M. Alkali activation of waste concrete powder: Effects of alkali type and concentration. Ceram Int 2023;49:16260–71.
[39] Reddy KC, Subramaniam KVL. Investigation on the roles of solution-based alkali and silica in activated low-calcium fly ash and slag blends. Cem Concr Compos 2021;123:104175.
[40] Sharma P, Gandhi PM, Chintersingh K-L, Schoenitz M, Dreizin EL, Liou S-C, Balasubramanian G. Accelerated intermetallic phase amorphization in a Mg-based high-entropy alloy powder. J Magnes Alloy 2024;12:1792–8.
[41] Shen Z, Zhu H, Zhao Z, Pang S, Li Z, Yang S, Cao P, Lin S. High-performance artificial aggregate prepared with recycled concrete powder and its impact on concrete properties. Constr Build Mater 2023;404:133151.
[42] Zhang T, Cui J, Chen M, Ouyang X, Yan Z. Effect of carbonated recycled concrete fines on early-age engineering properties, hydration and microstructure of cement paste under high substitution level and low water-to-binder ratio. J Build Eng 2024;96:110376.
[43] Gao H, Al-Damad IMA, Siddika A, Kim T, Foster S, Hajimohammadi A. Enhancing the workability retention of one-part alkali activated binders by adjusting the chemistry of the activators. Cem Concr Compos 2025;157:105928.
[44] Wang C, Tian Q, Zhang M, Ruan M, Zhao Z. Design and properties of ternary alkali-activated binder based on blast furnace slag, recycled powder and waste glass powder. J Environ Manag 2024;365:121685.
[45] Jiang Y, Li B, Liu S, He J, Hernandez AG. Role of recycled concrete powder as sand replacement in the properties of cement mortar. J Clean Prod 2022;371:133424.
[46] Chen D, Chen M, Zhang Y, Yang X, Zhang J, Zhao Y, Wu Y. Development of an environmental foamed concrete incorporating recycled cement concrete powder with carbonation. Constr Build Mater 2024;422:135833.
[47] Lee WKW, Deventer JSJ. Use of infrared spectroscopy to study geopolymerization of heterogeneous amorphous aluminosilicates. Langmuir 2003;19:8726–34.
[48] Garcia-Lodeiro I, Palomo A, Fernández-Jiménez A, Macphee DE. Compatibility studies between N-A-S-H and C-A-S-H gels. Study in the ternary diagram Na_2O–CaO–Al_2O_3–SiO_2–H_2O. Cem Concr Res 2011;41:923–31.
[49] Sun X, Liu J, Qiu J, Wu P, Zhao Y. Alkali activation of blast furnace slag using a carbonate-calcium carbide residue alkaline mixture to prepare cemented paste backfill. Constr Build Mater 2022;320:126234.
[50] Komnitsas K, Zaharaki D, Vlachou A, Bartzas G, Galetakis M. Effect of synthesis parameters on the quality of construction and demolition wastes (CDW) geopolymers. Adv Powder Technol 2015;26:368–76.
[51] Khater HM. Effect of calcium on geopolymerization of aluminosilicate wastes. J Mater Civ Eng 2012;24:92–101.
[52] Yuan B, Yu Q, Brouwers HJH. Evaluation of slag characteristics on the reaction kinetics and mechanical properties of Na_2CO_3 activated slag. Constr Build Mater 2017;131:334–46.
[53] Ahmari S, Xin R, Toufigh V, Zhang L. Production of geopolymeric binder from blended waste concrete powder and fly ash. Constr Build Mater 2012;35:718–29.
[54] Shi P, Falliano D, Yang Z, Marano GC, Briseghella B. Investigation on the anti-carbonation properties of alkali-activated slag concrete: effect of activator types and dosages. J Build Eng 2024;91:109552.
[55] Lu P, Li Q, Zhai J. Mineralogical characterizations and reaction path modeling of the pozzolanic reaction of fly ash–lime systems. J Am Ceram Soc 2008;91:955–64.
[56] Karam R, Bulteel D, Wattez T, Deneele D. Effect of marine sediments incorporation on the behaviour of alkali-activated GGBFS. Mater Struct 2019;52:110.
[57] Abdel daiem MM, Rashad AM, Said N, Abdel-Gawwad HA. An initial study about the effect of activated carbon nano-sheets from residual biomass of olive trees pellets on the properties of alkali-activated slag pastes. J Build Eng 2021;44:102661.
[58] Baggio TF, Possan E, Oliveira Andrade JJ. Physical-chemical characterization of construction and demolition waste powder with thermomechanical activation for use as supplementary cementitious material. Constr Build Mater 2024;437:136907.
[59] Ye H, Huang L, Chen Z. Influence of activator composition on the chloride binding capacity of alkali-activated slag. Cem Concr Compos 2019;104:103368.

[60] Gao H, Shikhov I, Hamed E, Hajimohammadi A, Al-Damad I, Arns C, Foster SJ. New insights on the basic creep mechanism of one-part alkali activated slag and fly ash paste. Cem Concr Res 2024;186:107691.
[61] Liu J, Tian Y, Ge X, Liu B, Liu K, Song G. Experimental study on MgO-Na_2CO_3 combined excitation recycled fine-powder-slag cementitious system and modification. Buildings 2024;14:592.
[62] Cheng Z, Wang K, Zhou J, Wu H. Mechanical properties evaluation of sustainable engineered cementitious composites containing recycled fine powders. J Build Eng 2023;71:106438.
[63] Xiao J, Hao L, Cao W, Ye T. Influence of recycled powder derived from waste concrete on mechanical and thermal properties of foam concrete. J Build Eng 2022; 61:105203.
[64] Horsakulthai V. Effect of recycled concrete powder on strength, electrical resistivity, and water absorption of self-compacting mortars. Case Stud Constr Mater 2021;15:e00725.
[65] Kim YJ, Choi YW. Utilization of waste concrete powder as a substitution material for cement. Constr Build Mater 2012;30:500–4.